

Cite this: *J. Mater. Chem. A*, 2018, 6, 24823Interplay between H₂O and CO₂ coadsorption and space-charge on Y-doped BaZrO₃ surfaces†Jonathan M. Polfus,  ‡*^{ab} Jing Yang  ‡^b and Bilge Yildiz*^{bc}

The present work quantifies the equilibrium defect and adsorbate chemistry on oxide surfaces in the presence of multiple gas components at elevated temperatures and sub-surface space charge. The concentrations of chemisorbed H₂O and CO₂ as well as surface protons and oxygen vacancies were calculated for Y-doped BaZrO₃ using a thermodynamic framework with input from first-principles calculations. The overall energy of the system was minimized based on contributions from gas adsorption, interactions between defects and adsorbates, segregation of point defects and space-charge formation, as well as configurational entropy. The coverage dependent adsorption energies were found as $-1.44 + 0.34\theta_{\text{H}_2\text{O}}$ eV and $-2.25 + 1.21\theta_{\text{CO}_2}$ eV for chemisorption of H₂O and CO₂, respectively. The interaction between the adsorbates was found to follow $1.72\theta_{\text{H}_2\text{O}}\theta_{\text{CO}_2}$ eV. The coverage of surface protons was above 0.3 up to 1000 K under most considered conditions (0.01–1 bar H₂O, 4×10^{-4} –1 bar CO₂) due to a favorable interaction with both surface hydroxide and CO₂ adsorbates. Most importantly, the results show that the coadsorption, adsorbate interactions or space-charge formation each played a major role in the obtained defect concentrations and surface coverages. Thus, the approach in this work demonstrates the importance of considering quantitatively each of these aspects in obtaining accurately the surface equilibria on complex catalytic oxides.

Received 1st October 2018
Accepted 16th November 2018

DOI: 10.1039/c8ta09491h

rsc.li/materials-a

1. Introduction

Perovskite oxides based on barium zirconate are applicable as proton conducting ceramic electrolytes for intermediate temperature fuel cells,^{1–4} electrolysis cells^{5,6} and electrochemical catalytic membrane reactors for steam-methane reforming⁷ and dehydrogenation processes.^{8,9} Most of these devices operate at temperatures from about 350 to 800 °C in H₂O and CO₂ containing atmospheres and the equilibrium surface chemistry can be expected to be significantly affected by the operating environment.^{10,11} It is therefore of importance to understand quantitatively how the surface composition and defect chemistry may influence the properties of the oxide surface for catalytic activity, chemical stability and coke resistance. For instance, Huang *et al.* recently demonstrated significantly enhanced CO₂ and H₂O exchange kinetics on oxide ion conducting perovskites and fluorites, as well as enhanced oxygen

exchange rates in the presence of H₂O or CO₂ in addition to O₂ on electronically conducting Sr-doped LaMnO₃.^{12,13} Duan *et al.*¹⁴ recently reported excellent performance and durability of BaZrO₃-based protonic ceramic fuel cells with a range of hydrocarbon fuels and a steam-to-carbon ratio of 2.5 : 1 at 500–600 °C.

As a proton conducting oxide, Y-doped BaZrO₃ (BZY) readily dissolves protons from water vapor by hydration of oxygen vacancies.¹⁵ Both the BaO and ZrO₂ terminations of the preferred (0 0 1) surface exhibit strong affinity for H₂O, and dissociative adsorption predominates according to computational studies.^{16,17} The hydroxide and protonic species remain at the surface at higher temperatures than in the bulk due to a more exothermic adsorption enthalpy compared to the bulk hydration enthalpy. Furthermore, these charged surface species, OH_{ad}⁺ and OH_O⁺ respectively in Kröger–Vink notation,¹⁸ are central in the formation of space-charge layers at the surface.^{19,20} In this respect, protons have been found to be particularly stable at the surface leading to a positive surface charge that is charge compensated by hydroxide adsorbates and a subsurface space-charge region.

Adsorption of CO₂ has recently been shown to be particularly exothermic for the (0 0 1) surfaces by chemisorption of carbonate species, CO₃²⁻.²¹ The calculated surface coverage as functions of temperature and p_{CO_2} showed that a full carbonate overlayer was stable under ambient 400 ppm CO₂ up to 400 K and that significant coverage could be retained up to 2000 K

*SINTEF Industry, Sustainable Energy Technology, PO Box 124 Blindern, NO-0314 Oslo, Norway. E-mail: jonathan.polfus@sintef.no

^aDepartment of Materials Science and Engineering, Massachusetts Institute of Technology, 77 Massachusetts Avenue, Cambridge, MA 02139, USA^bDepartment of Nuclear Science and Engineering, Massachusetts Institute of Technology, 77 Massachusetts Avenue, Cambridge, MA 02139, USA. E-mail: byildiz@mit.edu

† Electronic supplementary information (ESI) available. See DOI: 10.1039/c8ta09491h

‡ Equally contributing authors.



under 1 bar CO₂. While the overall chemical stability of bulk BaZrO₃ towards CO₂ has been demonstrated,^{21,22} recent studies have shown surface reactivity with CO₂ to form BaCO₃ by accommodating Ba-deficiency in the subsurface region.²³

Considering the strong adsorption of both H₂O and CO₂, interactions between the adsorbed species must be taken into account in order to appropriately describe the equilibrium surface coverages. Furthermore, the defect chemistry of the surface and subsurface must also be accounted for since all surface species – including neutral and charged adsorbates and point defects – interact and compete for the same surface sites. Accordingly, the gas adsorption equilibria will be influenced by the surface defect chemistry, and conversely the subsurface defect chemistry, or the space-charge region, will be affected by the adsorbates.

In the present work, we utilize first-principles calculations to investigate the concentration of adsorbates and defects on the BaO-terminated (0 0 1) surface of BZY under H₂O and CO₂ containing atmospheres. A thermodynamic model comprising gas adsorption equilibria, segregation of point defects and formation of a subsurface space-charge layer was implemented. As a result, surface coverages and subsurface space-charge behavior were obtained as a function of environmental variables. The individual contributions to the overall energy minimization of the system have been discussed in order to understand the interplay between gas adsorption equilibria and surface defect chemistry.

2. Computational approach

The DFT calculations were performed using VASP with the PBE generalized gradient approximation functional and projector-augmented wave pseudopotentials.^{24–26} The plane-wave cut-off energy was 500 eV and the *k*-point sampling was equivalent to 8 × 8 × 8 for the cubic BaZrO₃ unit cell. BaO-terminated (0 0 1) surfaces were constructed as symmetric 11-layer slabs. Adsorbates were considered at coverages of 0.11, 0.25, 0.5 and 1.0 with 2 × 2 and 3 × 3 expanded slabs (up to 243 atoms), and coadsorbate interaction was evaluated for equal coverages of 0.25 and 0.5 on 2 × 2 slabs, *i.e.*, half and full coverage, respectively. Y-acceptors were not explicitly included in the computational cells since the surface was BaO-terminated and any interactions between adsorbates and subsurface Y-dopants can be expected to be minor compared to interactions between adsorbates or between adsorbates and point defects. The adsorption thermodynamics were evaluated based on the adsorption energy, configurational entropy and vibrational properties of the adsorbates obtained by the finite displacement method. The adsorption energy, ΔE_i^{ads} , was calculated as the total energy differences of the adsorption reactions. The equilibrium constant of the adsorption reactions was given by

$$K = \exp\left(-\frac{\Delta H_i^{\text{ads}}}{kT}\right) \exp\left(\frac{\Delta S_i^{\text{ads}}}{T}\right) \quad (1)$$

where $\Delta H_i^{\text{ads}} = \Delta E_i^{\text{ads}}(\Theta_i) + \Delta ZPE$. Bulk parameters including a nominal Y-dopant concentration and surface segregation energies used for the thermodynamic model are listed in

Table 1 Bulk parameters (Y-dopant concentration, lattice constant, relative permittivity and enthalpy and entropy of hydration) and surface segregation energies of protons and oxygen vacancies used in the thermodynamic model

Y-dopant/mol%	20
Lattice constant/Å	4.214 (DFT)
ϵ_r	75 (exp) ²⁷
$\Delta H_{\text{hydration}}/\text{eV}$	−0.97 (exp) ¹
$\Delta S_{\text{hydration}}/\text{eV K}^{-1}$	−1.1 × 10 ^{−3} (exp) ¹
$\Delta E_{\text{OH}_0}^{\text{seg}}/\text{eV}$	−0.96 (DFT) ¹⁹
$\Delta E_{\text{V}_0}^{\text{seg}}/\text{eV}$	−0.42 (DFT) ¹⁹

Table 1. Further details can be found in our previous work on the same system.^{20,21}

The computed adsorption energies and segregation energies were fed into a thermodynamic framework to obtain the equilibrium concentrations of all adsorbates and defects by minimizing the total energy of the system.²⁸ Effects of defect interaction and formation of subsurface space-charge layers were taken into account.

The energy of the adsorption layer can be separated into the energy of H₂O adsorbates, CO₂ adsorbates and an interaction term. The energy of the H₂O/CO₂ adsorption layer without inter-adsorbate interactions was calculated by

$$E_i^{\text{ads}} = \Theta_i(\Delta H_i^{\text{ads}} - T\Delta S_i^{\text{ads}} - \Delta\mu_i) \quad (2)$$

where $\Delta\mu_i = kT \ln(p/p^0)$ is the chemical potential of the gas phase at varying partial pressure, and the coverage, Θ_i , represents the number of adsorbed molecules. The interaction between adsorbed H₂O and CO₂ was obtained from the difference in adsorption energy of the coadsorbates and the individual adsorbates (see Table 2), and described as

$$E_{\text{H}_2\text{O}-\text{CO}_2}^{\text{int}} = 1.72 \Theta_{\text{H}_2\text{O}} \Theta_{\text{CO}_2} \quad (3)$$

when the surface was considered to be neutral, *i.e.*, $\Theta_{\text{H}_2\text{O}}$ denoting paired surface proton and hydroxide species, OH₀⁺ and OH_{ad}[−], respectively. For charged surfaces, the concentration of excess surface protons segregated from bulk was defined as $\Theta_{\text{OH}_0}^{\text{exc}} = \Theta_{\text{OH}_0^+} - \Theta_{\text{OH}_{\text{ad}}^-}$ when $\Theta_{\text{OH}_0^+} > \Theta_{\text{OH}_{\text{ad}}^-}$, and zero otherwise. The $E_{\text{H}_2\text{O}-\text{CO}_2}^{\text{int}}$ interaction energy was then described as

Table 2 Energetics for dissociative adsorption of H₂O and chemisorption of CO₂ on pristine BaO-terminated BaZrO₃ (0 0 1) and parameters describing the interaction between surface species. The coverage dependent adsorption energies were obtained from linear fits with $R^2 = 0.999$ for CO₂ and $R^2 = 0.997$ for H₂O. The linear fit of $\Delta E_{\text{H}_2\text{O}-\text{CO}_2}^{\text{int}}$ according to eqn (3) showed $R^2 = 0.999$

	H ₂ O	CO ₂
$\Delta E_{\text{ads}}/\text{eV}$	−1.44 + 0.34 $\Theta_{\text{H}_2\text{O}}$	−2.25 + 1.21 Θ_{CO_2}
$\Delta ZPE/\text{eV}$	0.091	0.117
$\Delta S_{\text{ads}}/\text{eV K}^{-1}$	−6.37 × 10 ^{−4}	−8.78 × 10 ^{−4}
$\Delta E_{\text{H}_2\text{O}-\text{CO}_2}^{\text{int}}/\text{eV}$	1.72 $\Theta_{\text{H}_2\text{O}} \Theta_{\text{CO}_2}$	
$\Delta E_{\text{H}-\text{CO}_2}^{\text{int}}/\text{eV}$	−0.31 eV (ref. 21)	
Adsorption site	Ba + O	O



$$E_{\text{H}_2\text{O}-\text{CO}_2}^{\text{int}} = 1.72\Theta_{\text{OH}'_{\text{ad}}}\Theta_{\text{CO}_2} - 0.31\Theta_{\text{OH}'_0}^{\text{exc}}\Theta_{\text{CO}_2} \quad (4)$$

where the second term corresponds to a favorable interaction between surface protons and adsorbed CO_2 as determined in our previous work.²¹ The energies of the excess surface protons and oxygen vacancies were given by their segregation energies and electrostatic interaction with the surface potential, ϕ_0 , according to

$$E_{\text{OH}'_0}^{\text{exc}} = \Theta_{\text{OH}'_0}^{\text{exc}} \left(\Delta E_{\text{OH}'_0}^{\text{seg}} + e\phi_0 \right) \quad (5)$$

$$E_{V'_0}^{\text{seg}} = \Theta_{V'_0} \left(\Delta E_{V'_0}^{\text{seg}} + 2e\phi_0 \right) \quad (6)$$

where the coverage, Θ_i , represents the number of surface species. For a given surface potential the electrostatic potential distribution from surface to bulk was obtained by solving Poisson's equation

$$\varepsilon\varepsilon_0 \frac{d^2\phi}{dx^2} = -e \left(2c_{V'_0} + c_{\text{OH}'_0} - c_{Y'_{\text{Zr}}} \right) \quad (7)$$

where $c_{V'_0}$, $c_{\text{OH}'_0}$ and $c_{Y'_{\text{Zr}}}$ denote the subsurface concentrations of oxygen vacancies, protons and Y-dopants, respectively. V'_0 and OH'_0 were treated as mobile species that can redistribute within the space-charge region at distance x from the surface according to

$$c_i(x) = n_i \frac{\exp(\Delta E_i^f + q_i\phi(x))}{1 + \sum_{i'} \exp(\Delta E_{i'}^f + q_{i'}\phi(x))} \quad (8)$$

where i' denotes defect species that share the same site as c_i . The dopant species, Y'_{Zr} , were considered immobile with a fixed concentration of 0.2. The total energy of the space-charge layer was represented as

$$E_{\text{sc}} = \int_0^l \left(\sum_i c_i (\Delta E_i^f + q_i\phi) + \frac{1}{2} \varepsilon\varepsilon_0 \left(\frac{d\phi}{dx} \right)^2 \right) dx \quad (9)$$

where ΔE_i^f is the formation energy of each defect species and the space-charge layer extends a distance l into the bulk. The configurational entropy of all the surface species was calculated considering shared sites for CO_2 , OH'_0 and V'_0

$$\begin{aligned} S_{\text{config}} = & -k \left[\Theta_{\text{CO}_2} \ln \Theta_{\text{CO}_2} + \Theta_{\text{OH}'_0} \ln \Theta_{\text{OH}'_0} + \Theta_{\text{OH}'_{\text{ad}}} \ln \Theta_{\text{OH}'_{\text{ad}}} \right. \\ & + \Theta_{V'_0} \ln \Theta_{V'_0} + (1 - \Theta_{\text{CO}_2}) \ln(1 - \Theta_{\text{CO}_2}) + (1 - \Theta_{V'_0} \\ & - \Theta_{\text{OH}'_0} - \Theta_{\text{CO}_2}) \ln(1 - \Theta_{V'_0} - \Theta_{\text{OH}'_0} - \Theta_{\text{CO}_2}) + \left(1 \right. \\ & \left. - \Theta_{\text{OH}'_{\text{ad}}} \right) \ln(1 - \Theta_{\text{OH}'_{\text{ad}}}) \left. \right] \quad (10) \end{aligned}$$

The above set of equations form a thermodynamic framework describing the total energy of the system, including the adsorption layer, segregation layer and subsurface space-charge layer. The system was solved for each environmental condition (temperature and partial pressures) by variation of ϕ_0 to

minimize the total energy of the system, and thus obtain the equilibrium concentrations of surface defects and adsorbates, Θ_{CO_2} , $\Theta_{\text{OH}'_0}$, $\Theta_{\text{OH}'_{\text{ad}}}$ and $\Theta_{V'_0}$, the surface potential ϕ_0 , as well as the subsurface concentration profiles in a self-consistent way. The constraint for the energy minimization was the global charge neutrality condition

$$\sum_i q_i \Theta_i + \int_0^l q_j c_j dx = 0 \quad (11)$$

where Θ_i denotes charged adsorbates and surface defects, and c_j denotes defects in the subsurface space-charge region. Details on the implementation of the thermodynamic model and numerical solution scheme is provided in the ESI (Section 1†).

3. Results

Fig. 1 shows relaxed structures of dissociatively adsorbed H_2O on the BaO-terminated BaZrO_3 (0 0 1) surface at coverages from 0.11 to 1 monolayer. The H_2O adsorbate was found to be most stable with surface hydroxide, denoted OH'_{ad} , bridged between two barium, and surface protons, OH'_0 , directed towards the oxide ion of OH'_{ad} (Fig. 1a). The lowest energy configurations consisted of evenly spaced adsorbates at half coverage (Fig. 1b) and alternating rows with different symmetry at full coverage (Fig. 1c).

The interaction between H_2O and CO_2 adsorbates was evaluated for total surface coverages of 0.5 and 1. With respect to structural interactions, no significant changes were observed due to coadsorption of H_2O and CO_2 in the case of half coverage (Fig. 2a). On the other hand, a molecular H_2O adsorbate formed by association between OH'_{ad} and OH'_0 on the fully covered surface as shown in Fig. 2b.

The energetics of H_2O and CO_2 adsorption that comprise the main input from the first-principles calculations to the thermodynamic model are summarized in Table 2. The adsorption energy of H_2O ranged from -1.4 to -1.1 eV for coverages of 0.11 to 1, respectively. These values are similar albeit somewhat less exothermic than previously reported values of -1.5 to -1.3 eV for half and full coverage, respectively.¹⁶ Calculations for the ZrO_2 -terminated surface exhibited similar energies for dissociative adsorption of H_2O in range of -1.1 to -1.4 eV.^{17,20} The adsorption energy of CO_2 was more exothermic than that of H_2O at low coverage, -2.20 eV at $\Theta_{\text{CO}_2} = 0.06$. However, stronger adsorbate interactions resulted in a slightly lower adsorption energy for CO_2 than for H_2O at full coverage.²¹ The zero-point energy contribution to the adsorption enthalpy was quite small for both H_2O and CO_2 , which can be ascribed to the rather similar bond relationships for the adsorbed species and gaseous molecules.

The interaction energy between the coadsorbates, $E_{\text{H}_2\text{O}-\text{CO}_2}^{\text{int}}$, was found to be quite similar to the average interaction energy of the individual adsorbates from the coverage dependent adsorption enthalpies. For instance, the average increase in interaction energy from half to full coverage was 0.39 eV for adsorption of H_2O or CO_2 , and 0.43 eV in the case of coadsorption. It should be noted that the stabilizing interaction



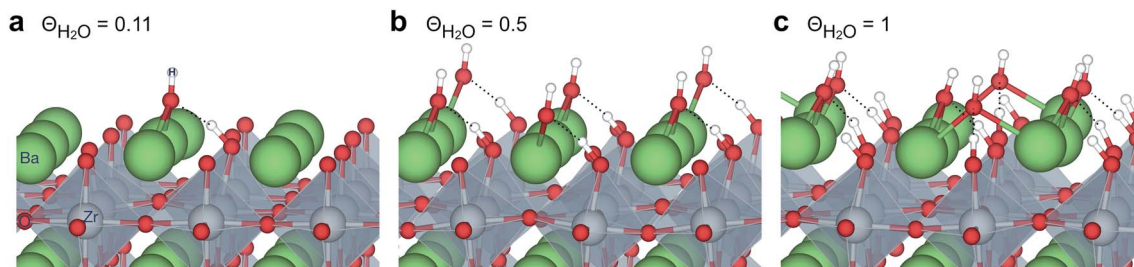


Fig. 1 Dissociatively adsorbed H_2O at coverages of (a) 0.11, (b) 0.5 and (c) 1 monolayer of the surface oxide ion sites on BaZrO_3 (0 0 1).

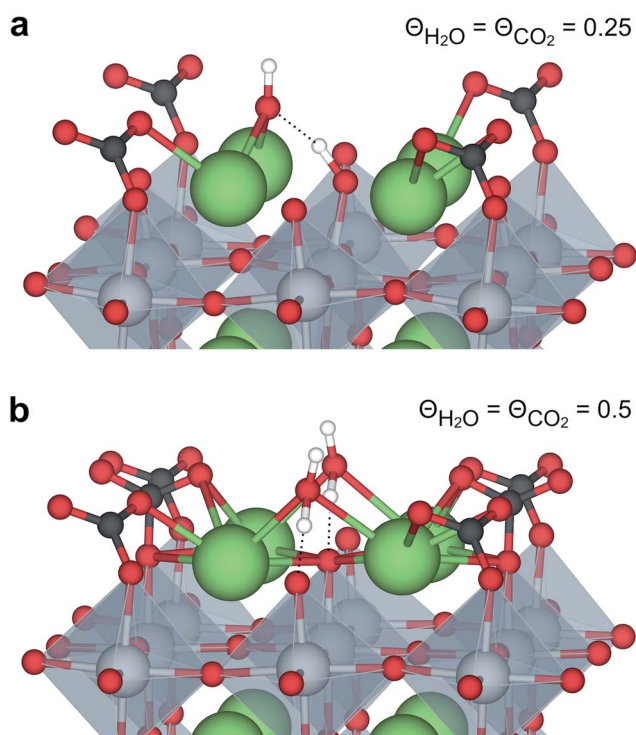


Fig. 2 Coadsorption of H_2O and CO_2 on BaZrO_3 (0 0 1) at total coverages of (a) 0.5 and (b) 1 monolayer.

between $\text{CO}_{2,\text{ad}}$ and OH'_0 , $E_{\text{H}-\text{CO}_2}^{\text{int}}$, only refers to excess OH'_0 since the interaction between OH'_0 and OH'_{ad} is included in the H_2O adsorption energy.

Fig. 3 shows the contributions to the overall energy of the $\text{BaZr}_{0.8}\text{Y}_{0.2}\text{O}_3$ system at equilibrium coverages as a function of temperature at ambient conditions, *i.e.*, 0.01 bar H_2O and 400 ppm CO_2 . The strong adsorption enthalpy of CO_2 predominates the stabilization of the system at temperatures below 800 K. Formation of the space-charge layer – driven mainly by the segregation of protons – also exhibits a significant contribution in this temperature range. Notably, the adsorption of H_2O is almost negligible despite the strongly exothermic adsorption of H_2O (see Table 2). This can be understood from the comparatively large interaction energy between H_2O and CO_2 , $\Delta E_{\text{H}_2\text{O}-\text{CO}_2}^{\text{int}}$, combined with the favorable coupling between $\text{CO}_{2,\text{ad}}$ and OH'_0 ($E_{\text{H}-\text{CO}_2}^{\text{int}}$). The configurational entropy plays an increasingly important role as temperature increases due to the

lower coverage and larger number of configurations of the surface species.

The calculated equilibrium coverages of adsorbates and defects are shown as a function of temperature in Fig. 4 including a subsurface space-charge with a corresponding potential. Under 1 bar H_2O and 400 ppm CO_2 , the surface is predominated by protons partly charge compensated by hydroxide, *i.e.*, dissociatively adsorbed H_2O and excess OH'_0 segregated from the bulk (Fig. 4a). The surface attains a positive charge over the whole temperature range with a potential of up to about 0.3 V mainly due to excess OH'_0 . The surface remained free of $\text{CO}_{2,\text{ad}}$ despite the strong adsorption enthalpy of CO_2 due to the unfavorable $E_{\text{H}_2\text{O}-\text{CO}_2}^{\text{int}}$ interaction term (Table 2). This behavior is shown graphically in contour maps of the contributions to the energy of the charge-neutral system spanning the complete ranges of $\Theta_{\text{H}_2\text{O}}$ and Θ_{CO_2} in Fig. S1 (ESI, Section 2†).

By reducing the H_2O pressure to 0.01 bar, Θ_{CO_2} predominates up to 800 K and remains significant to even higher temperatures (Fig. 4b). Protons become the predominant surface species above 800 K, but the coverage of OH'_{ad} is considerably lower which leads to a surface potential of up to 0.26 V at 500 K. At equal H_2O and CO_2 pressures of 1 bar, the surface is predominated by carbonate species up to about 1300 K (Fig. 4c).

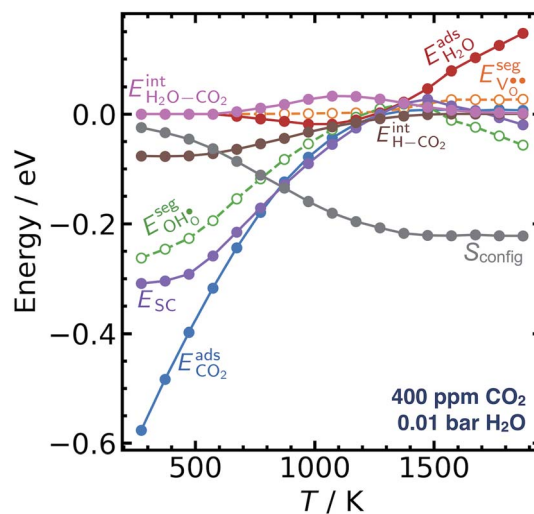


Fig. 3 Contributions from gas adsorption, space-charge, surface interactions and configurational entropy to the overall energy of the system at equilibrium coverages on $\text{BaZr}_{0.8}\text{Y}_{0.2}\text{O}_3$ (0 0 1) per unit cell.



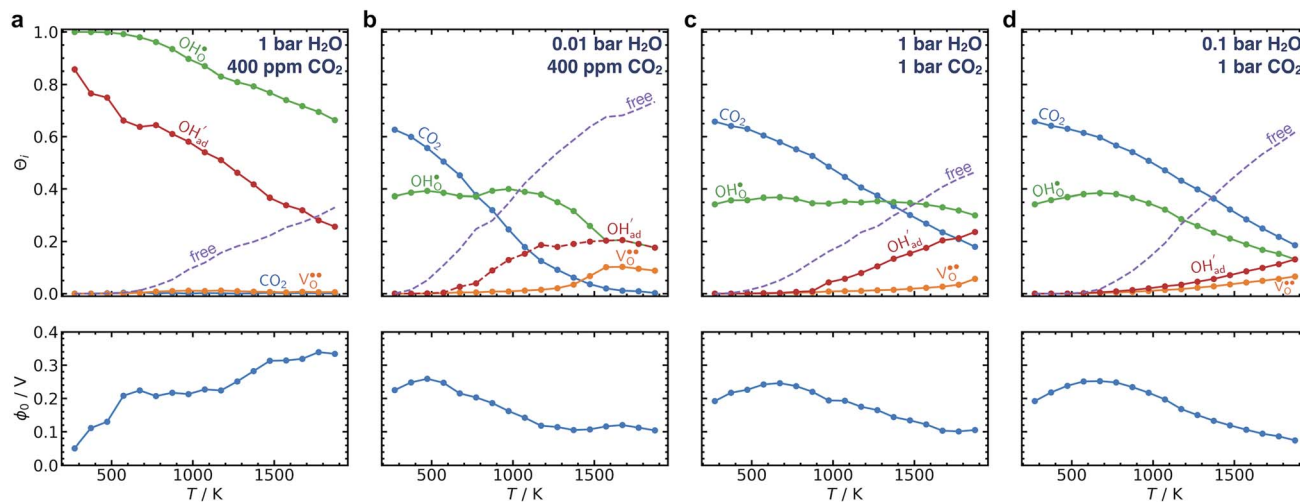


Fig. 4 Surface coverages of adsorbates and defects (protons, oxygen vacancies, hydroxide and carbonate species) as well as free surface sites (top) and the corresponding space-charge potential (bottom) on BaZr_{0.8}Y_{0.2}O₃ (0 0 1) as function of temperature under 1 bar H₂O, 400 ppm CO₂ (a), 0.01 bar H₂O, 400 ppm CO₂ (b) and 1 bar CO₂, 1 bar H₂O (c) and 0.1 bar H₂O, 1 bar CO₂ (d).

Fig. 4d shows a similar trend with 0.1 bar H₂O where CO_{2,ad} remains the predominant species over the whole temperature range.

Fig. 5 shows coverage isotherms at 1073 K as function of $p_{\text{H}_2\text{O}}$ and p_{CO_2} under 1 bar CO₂ and H₂O, respectively. Under these conditions, the coverage of CO₂ is negligible below 0.01 bar CO₂ (Fig. 5a). From Fig. 5b it becomes apparent that the space-charge potential to a large extent follows the segregation of OH'₀ with a significant contribution above 1×10^{-5} bar H₂O at this temperature. The potential increases with $p_{\text{H}_2\text{O}}$ up to a pressure of 1 bar where OH'_{ad} increasingly charge compensates the surface protons. Notably, the coverage of OH'_{ad} exhibits an inverse relationship with that of CO₂ as the coverage of OH'₀ surpasses θ_{CO_2} at around 0.5 bar H₂O (Fig. 5b). This behavior can be explained by the unfavorable interaction between CO₂ and OH'_{ad} (Eq. (4)).

Fig. 6 shows the concerted changes of the surface concentrations and the subsurface space-charge regions under 0.01 bar H₂O and 400 ppm CO₂ at 573–1473 K. The depletion of protons and oxygen vacancies in the subsurface space-charge region becomes less prominent as the potential is reduced from 0.25 V (Figure 6a) to 0.11 V (Fig. 6d). While the bulk becomes increasingly dehydrated above 573 K, segregated surface protons predominate the surface even at 1473 K due to the favorable proton segregation energy (Table 1). It has previously been shown that inclusion of an Y-segregation profile may significantly affect the space-charge properties of BZY surfaces and interfaces.^{20,29} In the present case, equilibration of Y'_{Zr} to the potential profile, *i.e.*, Gouy-Chapman approximation, lead to a slight increase in the potential while the surface proton concentration increased significantly at 1073 K in 1 bar H₂O and 1 bar CO₂ (Fig. S2, ESI Section 3†).

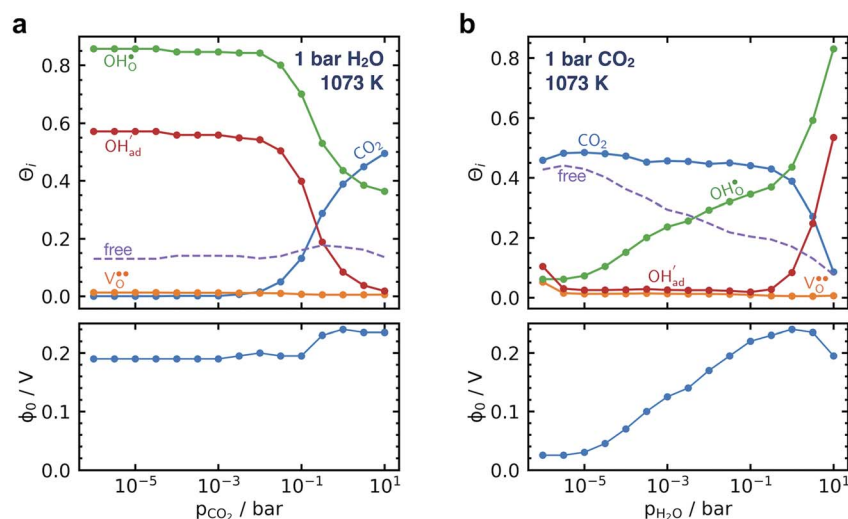


Fig. 5 Surface coverages of adsorbates, defects and free surface sites, and the corresponding space-charge potential on BaZr_{0.8}Y_{0.2}O₃ (0 0 1) at 1073 K as function of partial pressure of CO₂ (a) and H₂O (b) under 1 bar H₂O and CO₂, respectively.



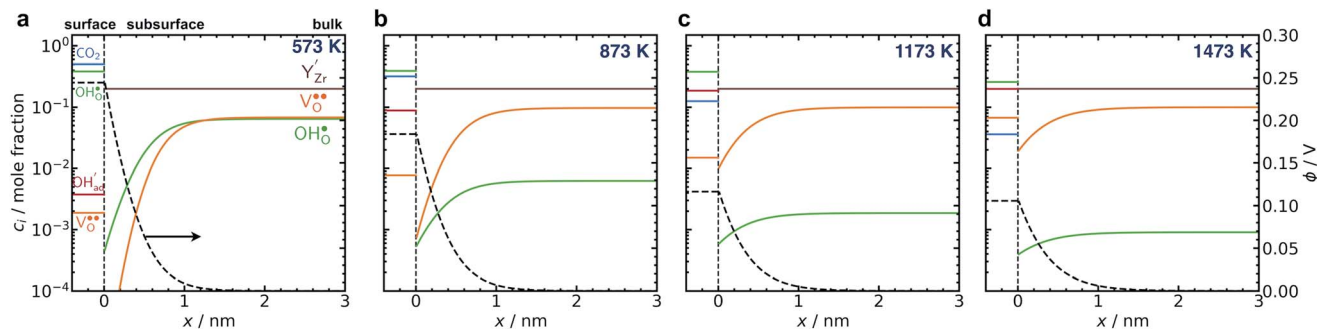


Fig. 6 Surface potential and concentration profile of defects and adsorbates from the surface layer on $\text{BaZr}_{0.8}\text{Y}_{0.2}\text{O}_3$ (0 0 1) ($x = 0$ nm) under 0.01 bar H_2O and 400 ppm CO_2 at 573 K (a), 873 K (b), 1173 K (c) and 1473 K (d).

4. Discussion

The present results show that interactions between coadsorbates, charged surface species and sub-surface space-charge formation can play a predominant role in the calculated surface coverages. The effect of not taking into account all aspects of the surface equilibria and space-charge formation is therefore evaluated next. Fig. 7 shows the calculated coverages at 1 bar H_2O and 1 bar CO_2 compared with coverages obtained without considering space-charge formation and without taking into account competitive adsorption of CO_2 . Without space-charge, the calculated surface coverage was dominated by chemisorbed H_2O since excess OH'_0 was not included in this model (Fig. 7a). On the other hand, in the absence of competitive CO_2 coadsorption, the surface was saturated by OH'_0 partly charge compensated by OH'_{ad} (Fig. 7b). It is clear that these shortcomings of not taking into account space-charge or

coadsorption significantly affect the calculated surface coverages in comparison to the results obtained with the complete model in Fig. 7c. By only considering space-charge formation in the absence of H_2O and CO_2 adsorbates (while OH'_0 was allowed due to segregation from bulk), a surface potential of 0.68 V was obtained due to a OH'_0 coverage of 0.66. Thus, it is clear that adsorption of uncharged gas species can also significantly affect the space-charge properties because of inter-adsorbate interactions and surface site limitations.

It was confirmed that the predominance of $\text{H}_2\text{O}_{\text{ad}}$ over $\text{CO}_{2,\text{ad}}$ obtained in Fig. 4a and 7a did not occur when removing the interaction between $\text{H}_2\text{O}_{\text{ad}}$ and $\text{CO}_{2,\text{ad}}$, *i.e.*, $E_{\text{H}_2\text{O}-\text{CO}_2}^{\text{int}} = 0$ eV. In this case, $\Theta_{\text{H}_2\text{O}}$ and Θ_{CO_2} were similar as expected due to their comparable adsorption energetics as well as the increased configurational entropy associated with coadsorption. These coverages were similar to those obtained by Tutuianu *et al.* for the structurally equivalent BaO (0 0 1) surface without

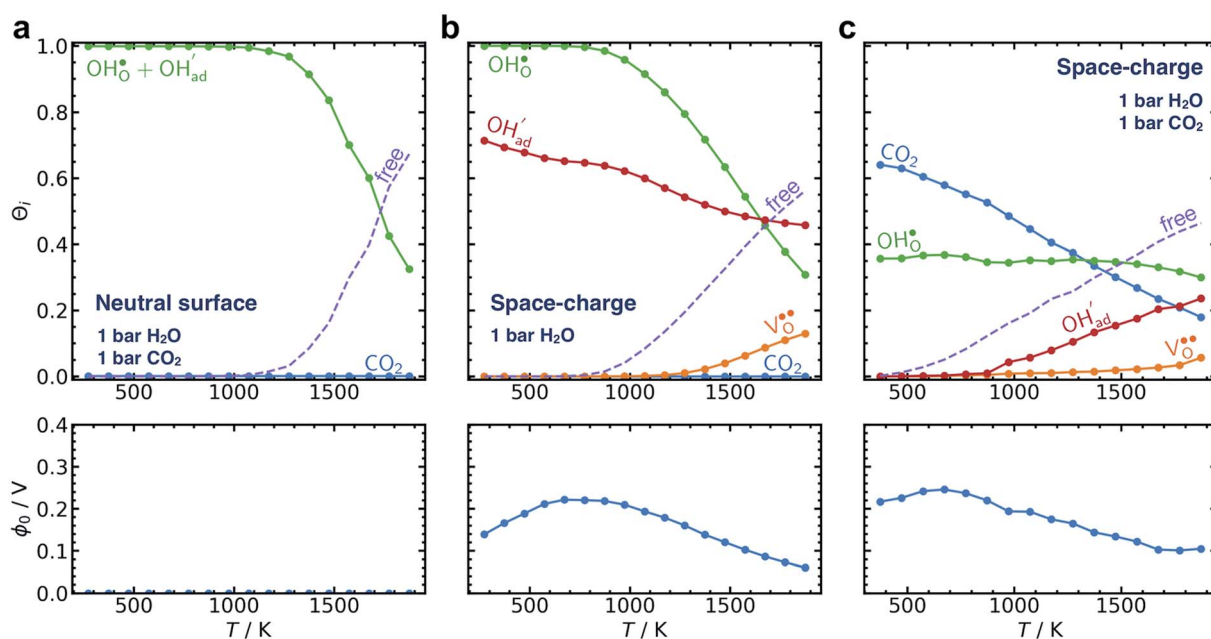


Fig. 7 Surface coverages of adsorbates and defects (protons, oxygen vacancies, hydroxide and carbonate species) as well as free surface sites and space-charge potential as function of temperature calculated without space-charge (a) and without competitive CO_2 adsorption (b) compared to the complete surface equilibria for $\text{BaZr}_{0.8}\text{Y}_{0.2}\text{O}_3$ (0 0 1) (c).



interactions between coadsorbates or surface defects.³⁰ However, Kwon *et al.* obtained a low interaction energy between chemisorbed H₂O and CO₂ on BaO (0 0 1) even for a total coverage of 0.5.³¹ The apparent difference in $E_{\text{H}_2\text{O}-\text{CO}_2}^{\text{int}}$ may be associated with a lower basicity of the BaO-terminated BaZrO₃ surface due to the presence of zirconium, which reduces the capacity for charge transfer to the adsorbates upon chemisorption.³¹

It is interesting to note that the calculated coverage of the OH'_{ad} adsorbate increases with temperature under some conditions (*e.g.*, Fig. 7c), which can seem counter intuitive due to the negative entropy of adsorption. Such behavior of OH'_{ad} has been predicted previously for BZY surfaces based on an increasingly positive space-charge potential at higher temperatures which thereby stabilized the negatively charged adsorbate.²⁰ However, the calculated space-charge potential becomes less positive at higher temperatures in the present work, and the increased OH'_{ad} coverage may instead be associated with the rather strong adsorbate interactions which become lower as Θ_{CO_2} decreases.

In terms of the functional properties of Y-doped BaZrO₃ as a proton conducting electrolyte, the present result show that the surface exhibits a high coverage of protons in the form of OH'_o under all the considered conditions. The presence of H₂O prevents the formation of a carbonate overlayer which is assumed to be detrimental to both performance and stability.^{21,23} Similar results were recently obtained for SrO-terminated SrTiO₃ based on DFT calculations and *in situ* FTIR analysis, although a relatively less exothermic chemisorption of CO₂ led to generally lower coverages of CO₂.³² The favorable interaction between surface OH'_o and CO_{2,ad} ($\Delta E_{\text{H}-\text{CO}_2}^{\text{int}}$) implies that there will be relatively large concentrations of protons available for incorporation into the electrolyte also in carbonate rich areas of the surface. The strong coadsorption may also correspond to an increased stability of the Y-doped BaZrO₃ surface with respect to formation of Ba(OH)₂ and BaCO₃, as well as coke deposition.¹⁴

5. Conclusion

The present work demonstrates quantitatively the crucial role of adsorbate interactions and space-charge formation simultaneously in determining the equilibrium surface chemistry of oxides in the presence of multiple gas components. Despite the favorable H₂O chemisorption on Y-doped BaZrO₃, the calculated H₂O coverage was quite low due to the more exothermic CO₂ chemisorption and unfavorable interaction between H₂O and CO₂ adsorbates. However, the coverage of surface protons was found to be considerable up to 1500 K under most conditions due to a favorable interaction with both hydroxide and CO₂ adsorbates. The calculated coverages were found to be significantly affected by the interactions between surface species, in particular between surface protons and CO₂. Competitive adsorption and space-charge formation were also determined to play major roles in the obtained coverages and concentration of defects.

Conflicts of interest

There are no conflicts to declare.

Acknowledgements

The Research Council of Norway is acknowledged for financial support through the FOXCET project (Nano2021, 228355), and the Norwegian CCS research centre (NCCS, 257579). Computational resources were provided through the NOTUR under the project nn9259k. J. Y. and B. Y. thank for support from the Consortium for Advanced Simulation of Light Water Reactors (CASL), an Energy Innovation Hub for Modeling and Simulation of Nuclear Reactors under U.S. Department of Energy Contract No. DE-AC05-00OR22725.

References

- 1 K. D. Kreuer, S. Adams, W. Münch, A. Fuchs, U. Klock and J. Maier, Proton Conducting Alkaline Earth Zirconates and Titanates for High Drain Electrochemical Applications, *Solid State Ionics*, 2001, **145**(1–4), 295–306.
- 2 Y. Yamazaki, R. Hernandez-Sanchez and S. M. Haile, High Total Proton Conductivity in Large-Grained Yttrium-Doped Barium Zirconate, *Chem. Mater.*, 2009, **21**(13), 2755–2762.
- 3 C. Duan, J. Tong, M. Shang, S. Nikodemski, M. Sanders, S. Ricote, A. Almansoori and R. O'Hayre, Readily Processed Protonic Ceramic Fuel Cells with High Performance at Low Temperatures, *Science*, 2015, **349**(6254), 1321–1326.
- 4 S. Choi, C. J. Kucharczyk, Y. Liang, X. Zhang, I. Takeuchi, H.-I. Ji and S. M. Haile, Exceptional Power Density and Stability at Intermediate Temperatures in Protonic Ceramic Fuel Cells, *Nat. Energy*, 2018, **3**, 202–210.
- 5 L. Bi, S. P. Shafi and E. Traversa, Y-Doped BaZrO₃ as a Chemically Stable Electrolyte for Proton-Conducting Solid Oxide Electrolysis Cells (SOECs), *J. Mater. Chem. A*, 2015, **3**, 5815–5819.
- 6 R. Strandbakke, E. Vøllestad, S. A. Robinson, M.-L. Fontaine and T. Norby, Ba_{0.5}Gd_{0.8}La_{0.7}CO₂O_{6.8} Infiltrated in Porous BaZr_{0.7}Ce_{0.2}Y_{0.1}O₃ Backbones as Electrode Material for Proton Ceramic Electrolytes, *J. Electrochem. Soc.*, 2017, **164**(4), F196–F202.
- 7 H. Malerød-Fjeld, D. Clark, I. Yuste-Tirados, R. Zanón, D. Catalán-Martinez, D. Beeff, S. H. Morejudo, P. K. Vestre, T. Norby, R. Haugrud, J. M. Serra and C. Kjølseth, Thermo-electrochemical production of compressed hydrogen from methane with near-zero energy loss, *Nat. Energy*, 2017, **2**, 923–931.
- 8 S. Hamakawa, T. Hibino and H. Iwahara, Electrochemical Methane Coupling Using Protonic Conductors, *J. Electrochem. Soc.*, 1993, **140**(2), 459–462.
- 9 S. H. Morejudo, R. Zanon, S. Escolastico, I. Yuste-Tirados, H. Malerød-Fjeld, P. K. Vestre, W. G. Coors, A. Martinez, T. Norby, J. M. Serra, *et al.*, Direct Conversion of Methane to Aromatics in a Catalytic Co-Ionic Membrane Reactor, *Science*, 2016, **353**(6299), 563–566.



- 10 Z. A. Feng, C. Balaji Gopal, X. Ye, Z. Guan, B. Jeong, E. Crumlin and W. C. Chueh, Origin of Overpotential-Dependent Surface Dipole at CeO_{2-x} /Gas Interface during Electrochemical Oxygen Insertion Reactions, *Chem. Mater.*, 2016, **28**(17), 6233–6242.
- 11 A. K. Opitz, A. Nenning, C. Rameshan, M. Kubicek, T. Götsch, R. Blume, M. Hävecker, A. Knop-Gericke, G. Rupprechter, B. Klötzer, *et al.*, The Surface Chemistry of Perovskite-Type Electrodes during High Temperature CO_2 Electrolysis Investigated by Operando Photoelectron Spectroscopy, *ACS Appl. Mater. Interfaces*, 2017, **9**(41), 35847–35860.
- 12 Y.-L. Huang, C. Pellegrinelli, A. Geller, S.-C. Liou, A. Jarry, L. Wang, Y. Yu, H. Bluhm, E. J. Crumlin, K. J. Gaskell, *et al.*, Direct Observation of Enhanced Water and Carbon Dioxide Reactivity on Multivalent Metal Oxides and Their Composites, *Energy Environ. Sci.*, 2017, 919–923.
- 13 Y.-L. Huang, C. Pellegrinelli and E. D. Wachsman, Oxygen Dissociation Kinetics of Concurrent Heterogeneous Reactions on Metal Oxides, *ACS Catal.*, 2017, **7**(9), 5766–5772.
- 14 C. Duan, R. J. Kee, H. Zhu, C. Karakaya, Y. Chen, S. Ricote, A. Jarry, E. J. Crumlin, D. Hook, R. Braun, *et al.*, Highly Durable, Coking and Sulfur Tolerant, Fuel-Flexible Protonic Ceramic Fuel Cells, *Nature*, 2018, **557**(7704), 217–222.
- 15 K. D. Kreuer, Aspects of the Formation and Mobility of Protonic Charge Carriers and the Stability of Perovskite-Type Oxides, *Solid State Ionics*, 1999, **125**(1), 285–302.
- 16 A. V. Bandura, R. A. Evarestov and D. D. Kuruch, Hybrid HF-DFT Modeling of Monolayer Water Adsorption on (001) Surface of Cubic BaHfO_3 and BaZrO_3 Crystals, *Surf. Sci.*, 2010, **604**(19–20), 1591–1597.
- 17 R. A. Evarestov and A. V. Bandura, LCAO Calculation of Water Adsorption on (001) Surface of Y-Doped BaZrO_3 , *Solid State Ionics*, 2011, **188**(1), 25–30.
- 18 F. A. Kröger and H. J. Vink, Relations between the Concentrations of Imperfections in Crystalline Solids, *Solid State Phys.*, 1956, **3**(C), 307–435.
- 19 J.-S. Kim, J.-H. Yang, B.-K. Kim and Y.-C. Kim, Proton Conduction at BaO-Terminated (001) BaZrO_3 Surface Using Density Functional Theory, *Solid State Ionics*, 2015, **275**, 19–22.
- 20 J. M. Polfus, T. S. Bjørheim, T. Norby and R. Bredesen, Surface Defect Chemistry of Y-Substituted and Hydrated BaZrO_3 with Subsurface Space-Charge Regions, *J. Mater. Chem. A*, 2016, **4**, 7437–7444.
- 21 J. M. Polfus, B. Yildiz, H. L. Tuller and R. Bredesen, Adsorption of CO_2 and Facile Carbonate Formation on BaZrO_3 Surfaces, *J. Phys. Chem. C*, 2018, **122**(1), 307–314.
- 22 K. H. Ryu and S. M. Haile, Chemical Stability and Proton Conductivity of Doped BaCeO_3 - BaZrO_3 Solid Solutions, *Solid State Ionics*, 1999, **125**(1), 355–367.
- 23 R. Sažinas, C. Bernuy-López, M.-A. Einarsrud and T. Grande, Effect of CO_2 Exposure on the Chemical Stability and Mechanical Properties of BaZrO_3 -Ceramics, *J. Am. Ceram. Soc.*, 2016, **99**(11), 3685–3695.
- 24 P. E. Blöchl, Projector Augmented-Wave Method, *Phys. Rev. B: Condens. Matter Mater. Phys.*, 1994, **50**(24), 17953–17979.
- 25 J. Perdew, K. Burke and M. Ernzerhof, Generalized Gradient Approximation Made Simple, *Phys. Rev. Lett.*, 1996, **77**(18), 3865–3868.
- 26 G. Kresse and D. Joubert, From Ultrasoft Pseudopotentials to the Projector Augmented-Wave Method, *Phys. Rev. B: Condens. Matter Mater. Phys.*, 1999, **59**(3), 1758–1775.
- 27 S. Ricote, N. Bonanos, A. Manerbino, N. P. Sullivan and W. G. Coors, Effects of the Fabrication Process on the Grain-Boundary Resistance in $\text{BaZr}_{0.9}\text{Y}_{0.1}\text{O}_{3-\delta}$, *J. Mater. Chem. A*, 2014, **2**(38), 16107–16115.
- 28 D. S. A. Mebane, Variational Approach to Surface Cation Segregation in Mixed Conducting Perovskites, *Comput. Mater. Sci.*, 2014, **103**, 231–236.
- 29 J. M. Polfus, T. Norby and R. Bredesen, Proton Segregation and Space-Charge at the BaZrO_3 (0 0 1)/ MgO (0 0 1) Heterointerface, *Solid State Ionics*, 2016, **297**, 77–81.
- 30 M. Tutuianu, O. R. Inderwildi, W. G. Bessler and J. Warnatz, Competitive Adsorption of NO , NO_2 , CO_2 , and H_2O on BaO (100): A Quantum Chemical Study, *J. Phys. Chem. B*, 2006, **110**(35), 17484–17492.
- 31 S.-C. Kwon, W.-R. Lee, H.-N. Lee, J.-H. Kim and H.-L. Lee, Competitive Adsorption of CO_2 and H_2O Molecules on the BaO (100) Surface: A First-Principle Study, *Bull. Korean Chem. Soc.*, 2011, **32**(3), 988–992.
- 32 A. Staykov, S. Fukumori, K. Yoshizawa, K. Sato, T. Ishihara and J. Kilner, Interaction of SrO-Terminated SrTiO_3 Surface with Oxygen, Carbon Dioxide, and Water, *J. Mater. Chem. A*, 2018, **6**, 22662–22672.

